Icarus 245 (2015) 145–152

Contents lists available at ScienceDirect

Icarus

journal homepage: www.elsevier.com/locate/icarus

Bulk chemical and Hf–W isotopic consequences of incomplete accretion during planet formation

Christina A. Dwyer [a,*], Francis Nimmo [a], John E. Chambers [b]

[a] University of California, Santa Cruz, 552 Red Hill Road, Earth and Planetary Sciences, Room A232, Santa Cruz, CA 95064, USA
[b] Dept. Terrestrial Magnetism, Carnegie Instit. Wash., Washington, DC 20015, USA

ARTICLE INFO

Article history:
Received 13 May 2014
Revised 6 September 2014
Accepted 8 September 2014

Keywords:
Impact processes
Planetary formation
Terrestrial planets

ABSTRACT

Late-stage accretion involves collisions which may result in complete or incomplete merging of the two objects, hit-and-run encounters, or mass loss from the target. We use a recent N-body study incorporating these different collision styles (Chambers, J.E. [2013]. Icarus 224, 43–56) to investigate how collision style affects the bulk chemical and isotopic outcomes of terrestrial planet formation. Compared with simulations in which all collisions result in perfect mergers, the variability in modeled silicate mass fraction and tungsten isotope anomaly is larger, especially for lower-mass planets. The final tungsten anomaly also shows a systematic reduction, because the timescale to finish planet growth is longer when incomplete mergers are included. Simulations including incomplete merging can reproduce the observed scatter in both tungsten anomaly and silicate mass fraction of the terrestrial planets.

1. Introduction

The final stages of terrestrial planet accretion involved energetic collisions between objects of comparable sizes. N-body simulations of this period have scored some notable successes, in particular obtaining accretion timescales which roughly agree with timescales inferred from the Hf–W isotopic system (Kleine et al., 2009), and generating model planetary systems which resemble our own inner Solar System (e.g., Agnor et al., 1999; Chambers, 2001; O'Brien et al., 2006; Raymond et al., 2006; Fischer and Ciesla, 2014). Recent work has focused on explaining the anomalously small mass of Mars (Hansen, 2009; Walsh et al., 2011), using the inferred mass of material delivered as a "late veneer" after the end of the giant impact phase as a chronometer (Jacobson et al., 2014), and examining the effect of spatial variations in starting compositions on the final make-up of planets (Bond et al., 2010; Rubie et al., submitted for publication).

Despite the success of these models, almost all make one major simplifying assumption, which is that all collisions result in a perfect merger. In reality, roughly one in two collisions will result in a "hit-and-run" outcome, rather than a merger (Asphaug, 2009; Kokubo and Genda, 2010) and most collisions are expected to result in at least some debris escaping the local environment. We refer to this process below as inefficient accretion or incomplete merging. As discussed below, incorporation of incomplete merging into N-body codes results in changes to the dynamics of the accreting bodies. In this paper, however, we focus on the compositional consequences of incomplete mergers, which have yet to be studied in any detail.

There are several lines of evidence suggesting the importance of incomplete mergers in the composition of own Solar System. Most notably, Mercury probably underwent a giant collision which removed most of its mantle (Benz et al., 2007), thus changing its bulk composition in a dramatic fashion. Alternatively, Mercury may be the remnants of an impactor which suffered a hit-and-run collision with a larger target body (Sarid et al., 2014; Asphaug and Reufer, 2014). The iron-poor Moon is probably a fragment of the Earth's mantle, spalled off during an impact (Ćuk and Stewart, 2012; Canup, 2012). There is thus little doubt that inefficient accretion can have a major effect on the bulk composition of the terrestrial planets. More subtly, trace element and isotopic systematics of planets can also be affected by inefficient accretion. For instance, O'Neill and Palme (2008) suggested that preferential removal of crustal material due to impact erosion would reduce the bulk concentrations of incompatible elements and thus render the bulk Earth non-chondritic.

In this paper we concentrate on two compositional aspects of inefficient accretion. The first is the bulk iron:silicate ratio of a body, since this can be remotely determined and provides a simple tracer of the effects of giant impacts. The second is the Hf–W

* Corresponding author.
E-mail addresses: cadwyer@ucsc.edu (C.A. Dwyer), fnimmo@es.ucsc.edu (F. Nimmo), chambers@dtm.ciw.edu (J.E. Chambers).

http://dx.doi.org/10.1016/j.icarus.2014.09.010
0019-1035/

isotopic system, which is strongly affected by the iron:silicate ratio, and also depends on the timescale with which accretion happens. Various authors have used the output of N-body simulations to calculate Hf–W isotopic evolution in the past (Halliday, 2004; Jacobsen, 2005; Nimmo and Agnor, 2006; Nimmo et al., 2010; Morishima et al., 2013; Kobayashi and Dauphas, 2013), but all such simulations have hitherto assumed perfect mergers.

Thanks to hydrocode simulations of individual impacts (Agnor and Asphaug, 2004; Leinhardt and Stewart, 2012) the outcome of an individual collision can be predicted, based on the impact velocity, impact angle, and relative and total masses of the two bodies involved. Kokubo and Genda (2010) incorporated a criterion based on these studies into an N-body code to investigate the effects of "hit-and-run" collisions on the timescale of accretion; their simulations included only perfect merger and hit-and-run collisions. As discussed further below, Chambers (2013) incorporated a more complex model of partial accretion into his N-body code, whereby a collision could result in one, two, or more final bodies, depending on the particular characteristics of the impact. The resulting dynamics change in two important ways, compared to simulations in which all collisions result in mergers. First, dynamical friction – which damps the eccentricities of larger bodies – plays a bigger role, because small objects are generated during impacts. Second, the timescale for accretion to be completed is increased by a factor of about two.

In this paper we use the results of Chambers (2013) to investigate the bulk chemical and isotopic consequences of inefficient accretion. The rest of this paper is organized as follows: in Section 2 we outline our computational approach, while in Section 3 we discuss the results, paying particular attention to how results differ between perfect-merger and incomplete-merger cases. In Section 4 we investigate the robustness of our results to various assumptions, while Section 5 summarizes our findings and makes suggestions for future work.

2. Methods

In this section, we detail the models used in this work. We briefly outline the N-body model (Section 2.1) of Chambers (2013), including the treatment of inefficient accretion. We then, in Section 2.2, describe our geochemical post-processing, in which the chemistry is evolved as a result of radioactive decay and impact-related mixing and partial equilibration. This post-processing stage is broken down into two parts: bulk composition (Section 2.2.1) and Hf–W isotopic (Section 2.2.2).

2.1. N-body model

16 runs were performed by Chambers (2013) using the Mercury N-body code (Chambers, 1999). Other than the incorporation of incomplete merging, this set-up is identical to Chambers (2001) (which assumed all collisions were perfect accretion events). As a result, we can compare the outcomes of the two groups of models directly, since the only difference is in the treatment of collisions. Hereafter, N-body data from the Chambers (2013) simulations (including runs with unimodal initial mass distribution as well as the bimodal runs discussed in that paper) will be referred to as Ch13 and N-body data from the Chambers (2001) simulations (freshly analyzed in this work) will be referred to as Ch01.

The initial bodies were distributed between 0.3 AU and 2.0 AU. The sixteen runs were divided into two groups (unimodal and bimodal initial mass distribution) which were each subdivided into two groups (identical initial masses and radially-dependent initial masses). Each run contained ≈150 initial bodies totaling 7.65×10^{-6} $M_\odot$ as well as Jupiter and Saturn in their current orbits with their current masses. In the radially-dependent cases, the initial mass distribution was defined such that the surface density is:

$$\Sigma(a) = \begin{cases} \left(6\ (0.7)^{-3/2}\ \mathrm{g/cm^2}\right)[(a/0.3\ \mathrm{AU}) - 1] & \text{for } a \in [0.3\ \mathrm{AU}, 0.7\ \mathrm{AU}] \\ (8\ \mathrm{g/cm^2})(a/1\ \mathrm{AU})^{-3/2} & \text{for } a \in [0.7\ \mathrm{AU}, 2\ \mathrm{AU}] \\ 0\ \mathrm{g/cm^2} & \text{for } a \notin [0.3\ \mathrm{AU}, 2\ \mathrm{AU}] \end{cases}$$

Runs 01–04: unimodal with uniform initial mass distribution; there were 153 planetesimals, each body was 5×10^{-8} $M_\odot$. *Runs 11–14:* unimodal with radially-dependent initial mass distribution; there were 158 planetesimals, the initial mass range was $[0.579, 11.8] \times 10^{-8}$ $M_\odot$. *Runs 21–24:* bimodal, uniform initial mass distribution; the planetesimals each had a mass of 2.8×10^{-8} $M_\odot$ and the embryos each had a mass of 28×10^{-8} $M_\odot$. *Runs 31–34:* bimodal, radially-dependent initial mass distribution with the same radial dependency as listed above. The initial planetesimal mass range was $[0.357, 6.66] \times 10^{-8}$ $M_\odot$ and the initial embryo mass range was $[14.3, 66.2] \times 10^{-8}$ $M_\odot$. Both bimodal runs had 154 initial bodies: 14 embryos (containing half the mass) and 140 planetesimals (containing half the mass).

Only the bimodal cases (Runs 21–34) were discussed in Chambers (2013) as the starting conditions of those simulations presumably more closely match the end conditions of oligarchic growth. We examine both cases here in order to gain insight into the extent to which the final results are sensitive to the initial conditions assumed. We exclude from consideration here any object which survived until the end of its simulation without experiencing any collisions. Specifically, these bodies (Planxxx) are, for Ch13: Plan139 of Run 24, Plan116 of Run 31, Plan75 of Run 33; and for Ch01: Plan127 of Run 01, Plan147 of Run 12, and Plan90 of Run 32.

When two bodies collide in Ch13, the outcome of the collision is dependent upon on the impact characteristics. The parameters which determine the mass(es) of the final body(ies) after an impact are impactor mass (M_i), target mass (M_t), mass ratio ($\gamma = M_\mathrm{i}/M_\mathrm{t}$), impact angle ($\theta$; head-on is 0°), and impact velocity (v_i). M_F is the mass of the largest final body post-impact and $M_\Sigma = M_\mathrm{t} + M_\mathrm{i}$ is the total mass of the colliding system.

The calculation steps are described in detail in Chambers (2013) and are based on Leinhardt and Stewart (2012). Briefly, the outcome depends on the size of the impact energy per unit mass, Q, and the specific energy required to disrupt 50% of the total mass, Q^*. A higher impact energy relative to the disruption energy results in a smaller largest remnant. The specific impact energy is given by

$$Q = \frac{\mu v_\mathrm{i}^2}{2(M_\mathrm{t} + M_\mathrm{i})}$$

where v_i is the impact velocity and the reduced mass $\mu = M_\mathrm{t}M_\mathrm{i}/(M_\mathrm{t} + M_\mathrm{i})$. For oblique impacts, the specific disruption energy is given by

$$Q^* = \left(\frac{\mu}{\mu_\alpha}\right)^{3/2} \left[\frac{(1+\gamma)^2}{4\gamma}\right] 1.44\pi\rho_1 G R_{c1}^2$$

Here $\rho_1 = 1$ g/cc is a reference density, $R_{c1}^3 = 3(M_\mathrm{t} + M_\mathrm{i})/(4\pi\rho_1)$ and μ_α is the reduced mass for the fraction α (Leinhardt and Stewart, 2012) of the projectile that would intersect the target in an oblique impact:

$$\mu_\alpha = \frac{\alpha M_\mathrm{t} M_\mathrm{i}}{M_\mathrm{t} + \alpha M_\mathrm{i}}$$

This approach allows the mass of both the largest remnant of the target and (if applicable) that of the projectile to be calculated. Mass in the target not accounted for is then divided up into one or more equal-mass collision fragments, with a minimum mass set to 0.0047 $M_\oplus$. Hit-and-run collisions are identified using the criterion

proposed in Asphaug (2010). In such cases the largest remnant is the original target (i.e., it is unaffected by the collision), but the projectile may suffer fragmentation.

2.2. Post-processing chemistry

We carry out our bulk chemical and isotopic calculations as a post-processing step, because the dynamics will not be affected by these kind of details. In Section 2.2.1 we discuss our approach to bulk composition, which is very similar to that adopted by Chambers (2013). We then use these results to calculate the Hf–W isotopic evolution of each body, as described in Section 2.2.2.

2.2.1. Bulk composition

We model all bodies as being composed of two idealized reservoirs, a metallic 'core' and a silicate 'mantle', and we track the masses of these compositional reservoirs for each body through the length of the simulation. We use a set of rules to determine the composition of the body or bodies produced in an impact as well as the fractions which come from the target and impactor. The largest post-collision body is labeled the LPCB and the smaller post-collision body or bodies are labeled SPCBs. A discussion of the ramifications of using different approaches for determining the compositional result of an impact can be found in Section 4.

All bodies are initially assigned a mantle mass fraction, y, of 0.7 which can subsequently be modified by impacts. Following Chambers (2013), the y value of the LPCB is determined by assembling the body from these reservoirs in this order until the body is complete: core of the target, core of the impactor, mantle of the target, mantle of the impactor. For partial accretion, this order is in line with smoothed particle hydrodynamics simulations (Asphaug and Reufer, 2013) and has been used elsewhere (Stewart and Leinhardt, 2012). For erosive impacts, this order probably overestimates the mantle loss (Marcus et al., 2010). If SPCBs are also present, they are built from the remainder of the material (in the case of multiple SPCBs, these all are given the same bulk composition and isotopic concentrations). In the case of a hit-and-run impact, the largest final body is identically the target. In some cases, hit-and-run impacts cause the impactor to split up into multiple fragments, in which case, the impactor is evenly divided amongst the fragments and no isotopic equilibration occurs (see below). For a perfect merger impact, the final body is simply composed of the entirety of the target and impactor.

2.2.2. Isotopic chemistry

The Hf–W isotopic system provides an important constraint on terrestrial planet accretion because it is sensitive to both the rate at which planets grow and the processes taking place during individual impacts (Kleine et al., 2009). Briefly, Hf is lithophile and W is siderophile, and ^{182}Hf decays to ^{182}W with a half-life of 9 Myr. Early core formation strips tungsten from the mantle; subsequent decay of ^{182}Hf results in a mantle enriched in ^{182}W compared with stable W isotopes (^{183}W and ^{184}W). As a result, the more enriched in ^{182}W the mantle is, the earlier core formation took place.

In reality, of course, core formation is not a single event, but rather core material is added during each collision. Furthermore, during each collision the core material added may isotopically re-equilibrate with the target mantle material, changing the mantle tungsten isotopic composition (Rubie et al., 2003). As a result, the dependence of the final mantle tungsten signature on the collision history is complex (e.g., Rudge et al., 2010; Nimmo et al., 2010). Nonetheless, by comparing simulations which differ only in their treatment of collisions, we can gain insight into how inefficient accretion is likely to affect the final isotopic outcome, as discussed below.

The partitioning of a specified element '*El*' between a metal reservoir '*met*' and a silicate reservoir '*sil*' at equilibrium is described by the elemental partition coefficient, D:

$$D_{\mathrm{El}} = \frac{[El]_{sil}}{[El]_{met}} \tag{1}$$

where $[El]_r$ is the concentration of element '*El*' in reservoir '*r*'. In this work, we use $D_{\mathrm{Hf}} = 10^4$ and $D_{\mathrm{W}} = 1/30$, which yield an Earth-like mantle $f^{Hf/W}$ for an Earth-like silicate mass fraction y. The partition coefficient also determines the concentration following initial differentiation. The elemental concentration in the silicate portion of a body, $[El]_{sil}$, immediately after differentiation is:

$$[El]_{sil} = \frac{[El]_{bulk}}{y + (1-y)/D_{\mathrm{El}}} \tag{2}$$

where $[El]_{bulk}$ is the bulk composition of the undifferentiated object. We assume D_{El} to be constant in time and space, and discuss the impact of this assumption in Section 5 below. The relative abundances of Hf and W is another constraint which can be measured in the laboratory. It is calculated using the stable isotopes in order to avoid the complications of attempting to deal with the radioisotopes and normalized against a chondritic undifferentiated reservoir, CHUR. Specifically, the Hf/W fractionation factor, $f^{Hf/W}$, relative to CHUR of a mantle reservoir m is:

$$f^{Hf/W} = \frac{\left([^{180}\mathrm{Hf}]/[^{183}\mathrm{W}]\right)_m}{\left([^{180}\mathrm{Hf}]/[^{183}\mathrm{W}]\right)_{\mathrm{CHUR}}} - 1 \tag{3}$$

The mantle tungsten anomaly, ϵ_{W}, is defined as follows:

$$\epsilon_{\mathrm{W}} = \left[\frac{\left([^{182}\mathrm{W}]/[^{183}\mathrm{W}]\right)_m}{\left([^{182}\mathrm{W}]/[^{183}\mathrm{W}]\right)_{\mathrm{CHUR}}} - 1\right] \times 10^4 \tag{4}$$

Here $[^{182}\mathrm{W}]$ and $[^{183}\mathrm{W}]$ are the concentrations of the two W isotopes, and m refers to the mantle reservoir. Between impacts, radioactive decay occurs.

The effect of a collision upon the Hf and W isotopes depends on the impact style. There are four types of impact styles discussed in this paper (total accretion, hit-and-run, partial accretion, basic erosion). A hit-and-run impact results in no change in isotopic chemistry for the target or the impactor. In the event that the impactor in the hit-and-run is split into multiple pieces, the isotopic concentrations of the SPBCs are identical to the original impactor (i.e., there is no interaction between the mantle and the core in a hit-and-run). In the case of a total accretion, partial accretion, or basic erosion collision, the isotopic composition of the post-collision body(ies) is/are calculated according to an idealized partial mixing model. This model is discussed below first for the case of a total accretion event and the modifications for the other collision styles follows.

An important parameter is the core re-equilibration factor, k, defined as the mass fraction of the impactor core which equilibrates with the silicates prior to mixing with the rest of the core material. Thus, $k = 1$ indicates complete re-equilibration, while $k = 0$ indicates that the core undergoes no exchange with the silicates. k is a free parameter; here we use $k = 0.4$ and discuss the effects of this assumption in Section 4.1 below.

In the case of a total accretion impact, the entirety of the target and the entirety of the impactor both end up in the LPCB. Let us label the target as "Body A" and the impactor as "Body B." Using this terminology, the isotopic compositions are calculated as follows:

1. The mantles from Body A and Body B are fully mixed. (We assume that the entire target mantle undergoes equilibration with the incoming core (cf., Sasaki and Abe, 2007; Morishima et al., 2013).)

2. The core from Body B is split into two parts according to the core re-equilibration factor k: 'Part a' contains a mass fraction k of the core and 'Part b' contains a mass fraction $(1-k)$ of the core and both portions have the same isotopic concentrations as did the original core of Body B.
3. Part a equilibrates fully with the combined mantle. Part b does not interact with any mantle material.
4. Part a and Part b and the core of Body A fully mix.

The method of calculating the concentrations of LPCB and SPCBs is the same for partial accretion and basic erosion impacts. This method is based upon that described above for total accretion impacts. The first step is to divide the impactor and target into "material going into the LPCB" and "material going into the SPCBs" according to Section 2.2.1. Note that this division does not alter the isotopic composition. To calculate the isotopic composition of the LPCB, label the material from the target as "Body A" and the material from the impactor as "Body B" and then follow the process described above for total accretion. To calculate the isotopic composition of the SPCBs, label the material from the target as "Body B" and the material from the impactor as "Body A" and then follow the process described above for total accretion – this is a "reverse impact" of the sort discussed by Leinhardt and Stewart (2012).

2.2.3. Parameters adopted

Bodies are assumed to start undifferentiated with chondritic compositions. The initial elemental ratios are taken to be as follows: $\left(\left[^{180}\mathrm{Hf}\right]/\left[^{183}\mathrm{W}\right]\right) = 2.836$, $\left(\left[^{182}\mathrm{Hf}\right]/\left[^{183}\mathrm{W}\right]\right) = 2.836 \times 10^{-4}$, and $\left(\left[^{182}\mathrm{W}\right]/\left[^{183}\mathrm{W}\right]\right) = 1.850664$; these values are taken from Jacobsen (2005). Bodies differentiate at 3×10^6 yr or when they undergo a non-hit-and-run impact, whichever occurs first. We assume that all bodies begin with an Earth-like value for y of 0.7. Note that the zero point of time in this work is the beginning of the simulation and is not tied into any specific event, such as CAI formation. For simplicity, we have set the zero time of the simulation to the formation of the Solar System, 4.567 Ga (from Amelin et al. (2002), cited within Jacobsen (2005)).

For simplicity, we assume that both the partition coefficients and k are constant in space and time, and examine the effects of varying these parameters below (Section 4). In reality, of course, neither assumption is likely to hold. Partition coefficients may vary spatially, because of the differing volatile contents and oxidation states of bodies originating from different regions (Bond et al., 2010; Schönbächler et al., 2010). Partition coefficients are also pressure- and temperature-dependent, and thus are expected to evolve during the growth of an individual object (Wood et al., 2006; Rubie et al., 2011; Siebert et al., 2013). Nonetheless, the integrated effect of this partitioning behavior has to match the known present-day mantle Hf–W ratio. As a result, assuming constant D values is a reasonable starting assumption, especially when our main focus is to investigate whether inefficient accretion changes the isotopic outcome.

The assumption of constant k is more problematic. If a constant k is assumed, the protracted timescale of planet formation in Ch13 combined with the measured ϵ_W data requires that equilibration be less than complete. Nimmo et al. (2010) concluded that intermediate k values ($\approx$0.5) are most consistent with the observations and, given the timescale found in this work, intermediate values are also consistent with Rudge et al. (2010). However both Nimmo et al. (2010) and Rudge et al. (2010) neglected the fact that k is likely to be strongly dependent on impact characteristics (Dahl and Stevenson, 2010; Deguen et al., 2014). Although it may ultimately be possible to calculate k for an individual impact (cf., Rubie et al., submitted for publication) the physics of emulsification and mixing during giant impacts is not currently well-understood, and we leave this issue as a topic for future work.

3. Results

3.1. General results

Fig. 1 shows the temporal evolution of four bodies which survive until the end of the simulation in Run 04, which is a unimodal, uniform initial mass distribution simulation. The x-axis is logarithmic, in units of Myr since the start of the simulation. Fig. 1a shows the mass of the labeled bodies over time. Although most collisions do not result in complete mergers, there is nonetheless a general increase in mass with time; there are occasional slightly erosive impacts but their effects are not visible on the scale of the plot. The first time at which a body reaches 68% of its final mass, t_{68}, is indicative of how rapidly accretion proceeds, though this timing cannot be readily related to the final tungsten anomaly (e.g., Fig. 3 of Nimmo and Kleine (2007)). The t_{68} of the bodies in Fig. 1 is: 51.1 Myr (Plan03), 72.8 Myr (Plan11), 53.0 Myr (Plan24), and 49.7 Myr (Plan56). Plan101 begins the simulation with 74% of its final mass.

Fig. 1b shows y, the silicate mass fraction, of the bodies. The original starting composition, $y_{init} = 0.7$, is marked with a magenta horizontal dash-dot-dot line. Impacts in which incomplete merging happens tend to decrease y, because core material is assumed to accrete preferentially (see Section 2.2 above). On the other hand, previously-produced mantle spall fragments will increase y when they are accreted. Because there does not appear to be a distinct trend in the evolution of y with time, this implies that the second mechanism (accretion of spall fragments) is of similar importance to the first.

Fig. 1c shows how ϵ_W of the silicate mantles evolves. The abrupt changes in ϵ_W are the result of impacts, while the background evolution is the result of radiogenic ingrowth (the curvature is a result of the log-linear plot). Generally, the result of an impact is to lower ϵ_W, because partial re-equilibration is being assumed ($k = 0.4$); however, occasionally an impact increases the target's ϵ_W. This occurs when the impactor mantle has a greater ϵ_W anomaly than

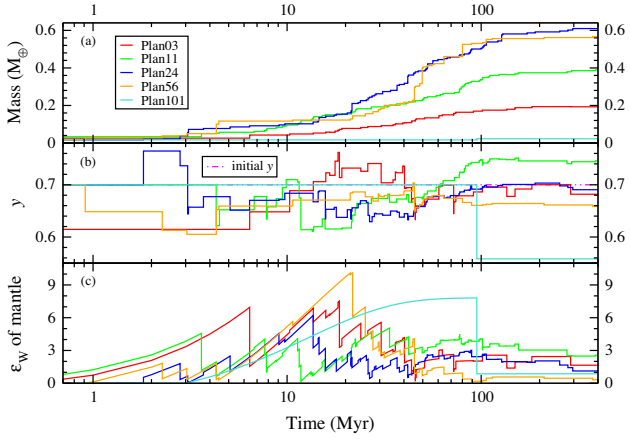

Fig. 1. Time history of surviving planetesimals from Run 04 (unimodal, uniform initial mass distribution). Final bodies are color-coded and labeled by their identification numbers assigned by the simulation. The zero point of time is the start of the simulation; it does not have an explicit physical meaning. Part (a) shows the mass of the body. There are some instances of mass decrease; however, they are not visible on the scale of this plot. The t_{68} of these bodies is: 51.1 Myr (Plan03), 72.8 Myr (Plan11), 53.0 Myr (Plan24), and 49.7 Myr (Plan56). Plan101 begins the simulation with 74% of its final mass. Part (b) shows y, the silicate mass fraction. The horizontal magenta dash-dot-dot line is $y_{init} = 0.7$. Part (c) shows ϵ_W of the silicate mantle. The curve for Plan101 has been scaled by a factor of 0.5 for plotting purposes. All parameters use nominal values ($k = 0.4$, $y_{init} = 0.7$). The concave upwards evolution of ϵ_W (most easily seen around $\sim$3 Myr) is a result of the log-linear plot. (For interpretation of the references to color in this figure legend, the reader is referred to the web version of this article.)

the target mantle and when the amount of the impactor mantle which mixes into the target is sufficiently large that neither mixing nor re-equilibration reduce the anomaly sufficiently. Impactors with a high mantle ϵ_W occur because an SPCB which was spalled off early and did not experience subsequent large impacts will have undergone significant radiogenic ingrowth.

Fig. 2 shows y as a function of mass for all the bodies surviving at the end of every simulation. The results are broken into unimodal and bimodal initial mass distributions, hollow circles for unimodal and asterisks for bimodal. For comparison, the measured values for terrestrial bodies are plotted in solid black circles. Fig. 2a shows the Ch13 bodies while Fig. 2b shows the Ch01 bodies (in which all collisions result in perfect mergers).

The model outcomes shown in Fig. 2a are approximately consistent with an envelope defined by the known planetary data. Importantly, there is more scatter in the outcomes at low masses. This is partly due to averaging effects – larger bodies have experienced more collisions – but may also be due to the fact that small bodies are inherently more vulnerable to experiencing mantle-stripping collisions than large ones (Agnor and Asphaug, 2004; Leinhardt and Stewart, 2012).

Fig. 2b shows no variation in y because every single collision is assumed to result in a perfect merger. The reason that the final Ch13 bodies tend to smaller masses when compared to Ch01 is likely a combination of two effects. First, there is an increase in dynamical friction (caused by the larger number of bodies present as a result of the multi-modal collisional model). This friction will circularize orbits, reducing the likelihood of late-stage collisions (which require crossing orbits) and reducing the mean mass of surviving bodies. Another factor contributing to the lower final masses is that Ch13 simulations lost more mass than did Ch01. The material lost from the system was either captured by the Sun or gravitationally ejected from the system at large. Table 1 shows that Ch13 has suffered more material loss and has less massive (and more numerous) surviving bodies than Ch01; as a result, both effects appear to have been operating.

Table 1
Properties of Ch01 and Ch13 simulations which are relevant to the determination of the cause of Ch13 having lower mass bodies. The average value and one standard deviation are reported. Note that this table excludes bodies which experienced no collisions and also excludes Run 31 of Ch13, which developed an apsidal resonance and thus lost an unusual amount of mass.

	Ch01	Ch13
Mass of a final body (10^{-6} $M_\odot$)	1.93 ± 0.092	1.21 ± 0.70
Number of final bodies per run	3.00 ± 0.73	4.40 ± 0.91
Fraction of mass which survives	0.752 ± 0.053	0.688 ± 0.038

Fig. 3 shows the mantle ϵ_W of all surviving bodies as a function of mass. The data is broken into unimodal and bimodal initial mass distributions, hollow circles for unimodal and asterisks for bimodal. Fig. 3a shows the Ch13 bodies while Fig. 3b shows the Ch01 bodies. Four data points (Earth, the shergottite (S) Mars source, the Moon and Vesta) are shown for comparison.

As with the silicate mass fraction (Fig. 2), our model results assuming incomplete accretion mostly fit within an envelope defined by the four data points. In particular, as discussed below, the models are capable of producing small bodies with a very wide range of ϵ_W values (e.g., both Moon and Vesta analogs are present), while at the larger masses the model ϵ_W numbers converge on Earth-like values.

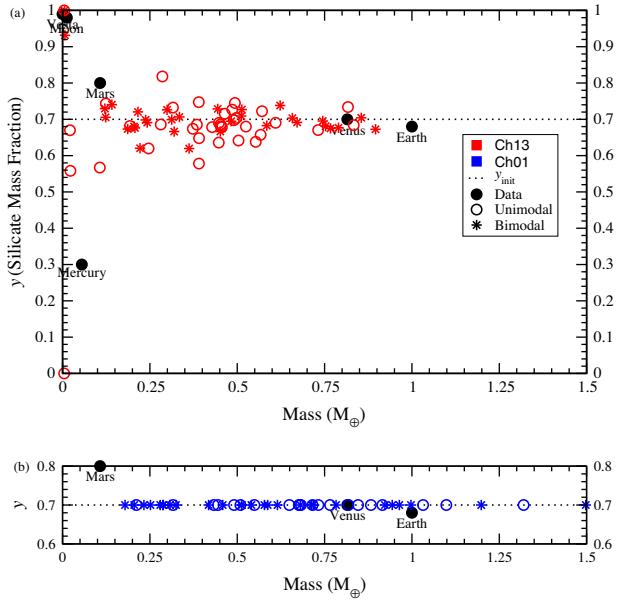

Fig. 2. The silicate mantle mass fraction (y) of all surviving bodies from all simulation runs as a function of mass. The solid black dots are data from our Solar System. The hollow dots are results from the unimodal initial mass distribution runs and the asterisks are from the bimodal initial mass distribution runs. Note that Vesta (4.3×10^{-5} $M_\oplus$) is significantly smaller than the minimum mass in the N-body code (0.0047 $M_\oplus$), and thus is not resolved by the simulations. Part (a) shows the Ch13 bodies, which used the multi-modal collisional model. Part (b) shows the Ch01 bodies, which required all collisions to be perfect mergers. Data for Vesta is from Russell et al. (2012).

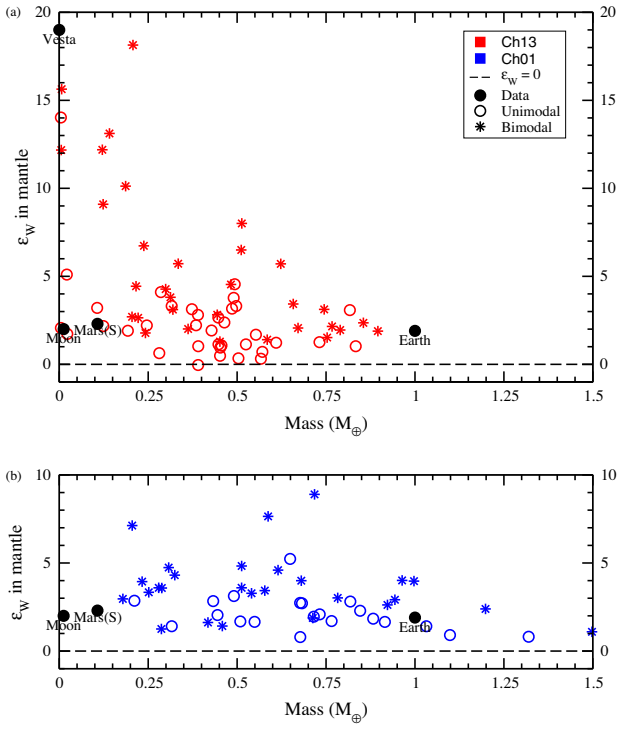

Fig. 3. The mantle tungsten isotopic anomaly (ϵ_W) of all surviving bodies from all simulation runs as a function of mass. The solid black dots are data from our Solar System. The hollow dots are results from the unimodal initial mass distribution runs and the asterisks are from the bimodal initial mass distribution runs. Note that Vesta is significantly smaller than the minimum mass permitted in our N-body code, and thus is not resolved by our simulations. Also, note that the Moon may have experienced partial or total equilibration with Earth during its formation and thus its datum might not be appropriate. Part (a) shows the Ch13 bodies, which used the multi-modal collisional model. Part (b) shows the Ch01 bodies, which required all collisions to be perfect mergers. The ϵ_W values for Earth, Moon, and Mars (S) were taken from Nimmo et al. (2010) and references therein. For Vesta, the ϵ_W value was taken from Jacobsen (2005) and the mass was from Russell et al. (2012).

Comparison between Fig. 3a (multi-modal collisions) and Fig. 3b (complete mergers) shows some important differences. First, there is much more scatter in ϵ_W when multi-modal collisions are permitted, especially at the lower mass range. This effect is mainly due to the fact that each impact tends to drive ϵ_W down (because of partial re-equilibration), and larger bodies have suffered more impacts. However, part of the explanation is that complete mergers only permit one pathway to generating a low-mass object (it experienced minimal collisions), while there is an additional pathway (spallation of a fragment from a larger target) available in our collisional model. Because these two pathways will in general produce quite different isotopic histories, one would expect to see more scatter in the multi-modal collisions case.

Fig. 3a also shows that lower ϵ_W values are obtained compared with Fig. 3b, and that in some cases slightly negative ϵ_W values result. The latter effect is impossible if all collisions result in perfect mergers. It arises because re-equilibration of impactor core material (which has a strongly negative ϵ_W) will drive the target mantle ϵ_W downwards, and will not necessarily be counteracted by the simultaneous addition of impactor mantle material if accretion is inefficient. A second effect which accounts for the ϵ_W values being slightly lower in the inefficient accretion case is the time taken for accretion to finish. As discussed in Section 1, inefficient accretion results in slower overall accretion timescales, which also tends to drive down the final tungsten anomaly (Jacobsen, 2005).

In both cases, the bimodal runs tend to produce slightly higher ϵ_W values than the unimodal runs. This is also probably a consequence of re-equilibration occurring during impacts. In the bimodal runs, some embryos have already formed, while in the unimodal runs there are no embryos initially present. As a result, the final planets in the unimodal runs tend to have experienced more impacts on average, and thus the final tungsten anomaly is more reduced.

3.2. Comparison with Solar System

Overall, the correlation between our Solar System and our simulation results (Figs. 2 and 3) is not perfect but it is encouraging and the agreement is better than perfect-merging-only simulations, showing the importance of using multi-modal collisions when investigating planet formation. Below we discuss how our results apply to each of the planets.

Mercury is extremely silicate poor, with $y \approx 0.3$. Aside from fragments which were entirely composed of core, the two most core-rich bodies in our simulations were Plan101 of Run 4, with $y = 0.56$, and Plan19 of Run 11, with $y = 0.57$. In order to better understand how these bodies end up with their low final y values, we have plotted their mass and y histories in Fig. 4. Plan101 experienced several hit-and-run collisions, while Plan19 underwent an accretionary collision with another body (Plan33) which had already suffered two mantle-removing impacts. We lack samples of the mercurian mantle to test for ϵ_W.

Venus lies within the y–M data cloud for Ch13 as well as Ch01. As we lack a measurement of ϵ_W for Venus, we cannot make other comparisons.

Technically, the binary Earth–Moon system should be treated as a combined set of constraints; however, as the N-body code does not include formation of binary planets, we consider Earth and Moon independently.

We have tuned our model to Earth, so it is unsurprising that we match the Earth well. For the Moon, the most important outcome of the multi-modal calculations is that it is relatively common to generate small fragments which – like the Moon – are mostly made of mantle material. Although we plot the lunar ϵ_W value, it is likely that post-impact isotopic equilibration between the Moon and the Earth took place (Pahlevan and Stevenson, 2007) so the significance of the Moon's ϵ_W value is unclear.

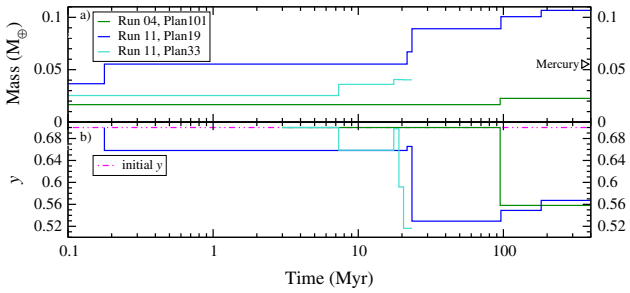

Fig. 4. The temporal history of the two bodies which have the closest y to Mercury: Plan101 of Run 04 and Plan19 of Run 11. Also plotted is Plan33 of Run 11, which is the impactor which collides with Plan19 at 23.4 Myr. The zero point of time is the start of the simulation; it does not have an explicit physical meaning. Part (a) shows the mass of the bodies. The mass of Mercury is labeled. For Plan19, $t_{68} = 23.4$ Myr; using the mass of Plan33 prior to its collision with Plan19 gives $t_{68} = 7.3$ Myr. Plan101 begins the simulation with 74% of its final mass. Part (b) shows y, the silicate mass fraction. The horizontal magenta dash-dot-dot line is $y_{init} = 0.7$. For Mercury, $y = 0.30$.

Mars is on the edge of the data cloud for y–M. While Mars does lie within the cloud of ϵ_W–M points, this comparison is misleading because the martian $f^{Hf/W}$ value is 3.38 ± 0.56 (Dauphas and Pourmand, 2011), much smaller than 12.9, the Earth-like value used in this work. Simultaneously matching both the terrestrial and martian $f^{Hf/W}$ values would require a time- or spatially-variable partition coefficient to be specified (cf., Nimmo et al., 2010).

The ϵ_W value listed for Vesta is from analyses of HED meteorites. Vesta is much less massive than the minimum mass permitted in our N-body code (4.3×10^{-5} $M_\oplus$ versus 4.7×10^{-3} $M_\oplus$). Nonetheless, it is likely that higher-resolution simulations, permitting lower masses, would still result in fragments that underwent early differentiation and were not incorporated into a larger body subsequently. It is these kinds of fragments that generate Vesta-like ϵ_W values.

4. Sensitivity analysis

We may summarize the results of this study relatively simply. First, models in which incomplete accretion is included are more successful in matching the observed scatter in both y and ϵ_W in Solar System bodies (Figs. 2 and 3). Second, these same models produce outcomes which are more diverse at lower masses. This increasing diversity is partly a result of the effect of averaging for larger bodies, but for ϵ_W also arises because objects exposed to fewer impacts have undergone less re-equilibration and can thus retain large tungsten anomalies.

Below, we investigate the extent to which these results depend on the various assumptions and parameter choices made. In general, we find that although there are some quantitative differences, the qualitative results appear robust.

4.1. Re-equilibration factor k

For simplicity, we assumed a constant value for the equilibration factor k. In reality, this quantity is likely to depend on the details of individual impacts (Section 2.2.3). In Fig. 5 we plot how the mean mantle ϵ_W of Earth-like bodies varies with the value of k assumed. As one would expect, more re-equilibration (higher k) results in lower final tungsten anomalies. The inefficient accretion cases have a slightly lower mean ϵ_W value than the complete merger cases, because the timescale to complete accretion is longer for the former (see above). The trend is similar for small

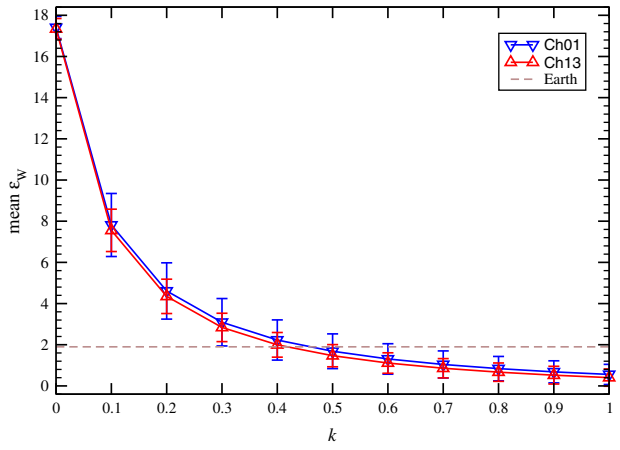

Fig. 5. The mean mantle ϵ_W of final bodies in each simulation style. Only bodies with mass $\geqslant 0.75\ M_\oplus$ are plotted. The error bars shown are one standard deviation. The blue line with down triangles is Ch01 and the red line with up triangles is Ch13. The horizontal brown dashed line is ϵ_W of Earth. 15 bodies from Ch01 made the mass cut-off and 7 bodies from Ch13 made the mass cut-off. (For interpretation of the references to color in this figure legend, the reader is referred to the web version of this article.)

bodies, however their mean ϵ_W is higher and they have a larger standard deviation by a factor of several. Additionally, in the small bodies, Ch01 has smaller standard deviation than Ch13 for the same mass cut-off. To match the measured ϵ_W value for the Earth, a k in the range 0.3–0.6 is required, which is compatible with the ranges obtained by Rudge et al. (2010) and Nimmo et al. (2010).

4.2. Initial silicate mass fraction y_{init}

For our nominal model we chose $y_{init} = 0.7$ because that is close to the present-day value of Earth and Venus. For comparison, we also examined the case where $y_{init} = 0.6$ was used. Although a reduction in y_{init} made it easier to generate Mercury-like outcomes (with low y values), it made Earth- or Mars-like core mass fractions very difficult to obtain. With $y_{init} = 0.6$, the final y values for Ch13 were depressed by 0.10 on average, for large bodies only (mass $> 0.75\ M_\oplus$) and for all bodies. For Ch13, there are seven large bodies and 68 bodies total while for Ch01, there are fifteen large bodies and 48 total.

In order to determine the effect of changing y_{init} on ϵ_W, D_W must be adjusted in order to generate the required $f^{Hf/W}$. As D_{Hf} is very large, we may use Eq. (49) of Jacobsen (2005) to determine the D_W value adjusted to account for using a modified y_{init} value:

$$D'_W \approx D^\circ_W \frac{(1 - y^\circ_{init}) y'_{init}}{(1 - y'_{init}) y^\circ_{init}} \quad (5)$$

where the $'$ superscript denotes the modified value and the $^\circ$ superscript denotes the nominal value. Using this equation, $y'_{init} = 0.6$ gives $D'_W = 7/135$.

For the large bodies of Ch13, the $y_{init} = 0.6$ case depressed the average ϵ_W value by 0.062 ± 0.101 ϵ_W units (one standard deviation) compared to $y_{init} = 0.7$ and for the entire population of Ch13, the average ϵ_W was increased by 0.13 ± 0.26 ϵ_W units. Neither of these are significantly different from zero change. In all cases, there was less scatter in ϵ_W using the lower y_{init} value. For Ch01, there was no change in ϵ_W compared to their nominal values.

The minimal effect of changing y_{init} may be understood by considering the simple two-stage core formation scenario (Jacobsen, 2005). In this situation, the final ϵ_W value depends only on the core formation time and $f^{Hf/W}$. Since we have maintained $f^{Hf/W}$ at the same value, and the time-sequence of impacts is unchanged, it is not surprising that there is little effect on ϵ_W. The small deviations in the Ch13 case are the result of variations in the silicate mass fraction due to multi-modal collisions.

4.3. Differentiation time t_{diff}

For our nominal calculations we assumed that the time of differentiation t_{diff} is either 3 Myr after the start of the simulation or the time of the first non-hit-and-run impact. A 3 Myr delay after CAI formation is broadly consistent with the onset of extensive silicate melting due to ^{26}Al decay, but the zero-time of our model is probably later than CAI formation (because significant planet growth has already occurred). To test the effect of our choice for t_{diff} on our results, we also ran our simulation using $t_{diff} = 0$ and found that the results were not significantly different. The mean change was 0.39 ± 0.58 ϵ_W units (one standard deviation) and the range was $[-0.079, 4.06]$ ϵ_W units, but only four bodies were changed by more than 0.75 ϵ_W units. Given the intrinsic variability in the outcomes (Fig. 3), these small variations are unlikely to matter.

5. Discussion and conclusions

N-body calculations in which not all collisions result in perfect mergers provide a more accurate depiction of the likely processes occurring during the final stages of planetary accretion (Chambers, 2013). In this work, we have carried out an initial analysis of how inefficient merging affects the chemical and isotopic evolution of the terrestrial planets. The biggest effect of including inefficient merging is an increased scatter in both model silicate mass fraction and mantle ϵ_W. The scatter is larger at small masses, mainly because of the averaging effects of multiple impacts (and, for ϵ_W, additional re-equilibration). The model predictions for both y and ϵ_W match the measured values quite well when incomplete merging is included (Figs. 2 and 3). Inefficient merging also results in a longer timescale to complete accretion, which slightly reduces the final mantle tungsten anomaly ϵ_W of the terrestrial planets (Fig. 3).

There are several obvious future avenues of investigation. One is to improve the chemical model used here. For instance, we could follow the approach of Rubie et al. (submitted for publication) and adopt a more complicated (and hopefully realistic) prescription for k and the relevant partition coefficients D. Although any successful prescription for D has to produce the present-day mantle concentrations, there are different models for how D varies with time (e.g., Siebert et al., 2013), and they may produce different ϵ_W outcomes. Likewise, k probably varies with impactor size, and so too may the fraction of the mantle which initially equilibrates with the impactor (an effect not investigated here). A second avenue is to investigate the role of spatial variations in the starting conditions. Several lines of evidence suggest that later impactors were probably derived from greater semi-major axes and were more volatile-rich and more oxidized (O'Brien et al., 2006; Schönbächler et al., 2010; Rubie et al., 2011) than earlier impactors; the extent to which this kind of variation might affect tungsten isotopic evolution has yet to be determined. One way of simultaneously matching $f^{Hf/W}$ as well as ϵ_W for Earth and Mars is to assume some initial spatial variation in partitioning behavior (e.g., Fig. 1a of Nimmo et al. (2010)).

The other obvious direction is to examine the effects of different accretion scenarios. Our simulations assume Jupiter and Saturn are in their current orbit during terrestrial planet formation; however, recent work has proposed a 'Grand Tack' model wherein Jupiter migrated extensively during the formation of the Solar System, with potentially dramatic effects on the terrestrial planet forming region (Walsh et al., 2011). At present, the Grand Tack simulations treat all impacts as perfect mergers, but this may be rectified in

future work, at which point the chemical and isotopic consequences can be examined. Another detail to include would be mantle stripping of impactors during hit-and-run collisions, as has been proposed as an origin for Mercury (Sarid et al., 2014; Asphaug and Reufer, 2014). Permitting the formation of binary planets (such as the Earth–Moon system) would allow for better comparison between simulation results and our Solar System. Lastly, advances in high-performance computing will allow more realistic simulations to be run. Using a larger number of starting bodies and allowing smaller fragments in the N-body code would be desirable, as is carrying out large numbers of realizations (Fischer and Ciesla, 2014). Extending the time period covered by simulations to earlier in planet formation (e.g., oligarchic or runaway growth) would improve our ability to test our understanding of formational process and could permit the inclusion of Mars, Vesta, and meteorites as constraints. It will also soon be possible to resolve crustal layers in impact simulations, the results of which can ultimately be incorporated into N-body codes. It will therefore soon be possible to investigate the suggestion by O'Neill and Palme (2008) that crustal erosion significantly altered the elemental composition of the Earth.

Acknowledgments

This work was supported by NASA-NNX11AK60G, a UCSC Cota-Robles Fellowship, and an ERC Advanced Grant "ACCRETE" (contract number 290568). We thank John Rudge and an anonymous reviewer for their thoughtful comments.

References

Agnor, C., Asphaug, E., 2004. Accretion efficiency during planetary collisions. Astrophys. J. 613, L157–L160.
Agnor, C.B., Canup, R.M., Levison, H.F., 1999. On the character and consequences of large impacts in the late stage of terrestrial planet formation. Icarus 142, 219–237.
Amelin, Y., Krot, A.N., Hutcheon, I.D., Ulyanov, A.A., 2002. Lead isotopic ages of chondrules and calcium–aluminum-rich inclusions. Science 297, 1678–1683.
Asphaug, E., 2009. Growth and evolution of asteroids. Ann. Rev. Earth Planet. Sci. 37, 413–448.
Asphaug, E., 2010. Similar-sized collisions and the diversity of planets. Chemie der Erde/Geochem. 70, 199–219.
Asphaug, E., Reufer, A., 2013. Late origin of the Saturn system. Icarus 223, 544–565.
Asphaug, E., Reufer, A., 2014. Mercury and other iron-rich planetary bodies as relics of inefficient accretion. Nat. Geosci. 7, 564–568.
Benz, W., Anic, A., Horner, J., Whitby, J.A., 2007. The origin of Mercury. Space Sci. Rev. 132, 189–202.
Bond, J.C., Lauretta, D.S., O'Brien, D.P., 2010. Making the Earth: Combining dynamics and chemistry in the Solar System. Icarus 205, 321–337.
Canup, R.M., 2012. Forming a Moon with an Earth-like composition via a giant impact. Science 338, 1052–1055.
Chambers, J.E., 1999. A hybrid symplectic integrator that permits close encounters between massive bodies. Mon. Not. R. Astron. Soc. 304, 793–799.
Chambers, J.E., 2001. Making more terrestrial planets. Icarus 152, 205–224.
Chambers, J.E., 2013. Late-stage planetary accretion including hit-and-run collisions and fragmentation. Icarus 224, 43–56.
Ćuk, M., Stewart, S.T., 2012. Making the Moon from a fast-spinning Earth: A giant impact followed by resonant despinning. Science 338, 1047–1052.
Dahl, T.W., Stevenson, D.J., 2010. Turbulent mixing of metal and silicate during planet accretion – And interpretation of the Hf–W chronometer. Earth Planet. Sci. Lett. 295, 177–186.
Dauphas, N., Pourmand, A., 2011. Hf–W–Th evidence for rapid growth of Mars and its status as a planetary embryo. Nature 473, 489–492.
Deguen, R., Landeau, M., Olson, P., 2014. Turbulent metal-silicate mixing, fragmentation, and equilibration in magma oceans. Earth Planet. Sci. Lett. 391, 274–287.
Fischer, R.A., Ciesla, F.J., 2014. Dynamics of the terrestrial planets from a large number of N-body simulations. Earth Planet. Sci. Lett. 392, 28–38.
Halliday, A.N., 2004. Mixing, volatile loss and compositional change during impact-driven accretion of the Earth. Nature 427, 505–509.
Hansen, B.M.S., 2009. Formation of the terrestrial planets from a narrow annulus. Astrophys. J. 703, 1131–1140.
Jacobsen, S.B., 2005. The Hf–W isotopic system and the origin of the Earth and Moon. Ann. Rev. Earth Planet. Sci. 33, 531–570.
Jacobson, S.A., Morbidelli, A., Raymond, S.N., O'Brien, D.P., Walsh, K.J., Rubie, D.C., 2014. Highly siderophile elements in Earth's mantle as a clock for the Moon-forming impact. Nature 508, 84–87.
Kleine, T. et al., 2009. Hf–W chronology of the accretion and early evolution of asteroids and terrestrial planets. Geochim. Cosmochim. Acta 73, 5150–5188.
Kobayashi, H., Dauphas, N., 2013. Small planetesimals in a massive disk formed Mars. Icarus 225, 122–130.
Kokubo, E., Genda, H., 2010. Formation of terrestrial planets from protoplanets under a realistic accretion condition. Astrophys. J. 714, L21–L25.
Leinhardt, Z.M., Stewart, S.T., 2012. Collisions between gravity-dominated bodies. I. Outcome regimes and scaling laws. Astrophys. J. 745, 79-1–79-27 (article number 79).
Marcus, R.A., Sasselov, D., Stewart, S.T., Hernquist, L., 2010. Water/icy super-Earths: Giant impacts and maximum water content. Astrophys. J. 719, L45–L49.
Morishima, R., Golabek, G.J., Samuel, H., 2013. N-body simulations of oligarchic growth of Mars: Implications for Hf–W chronology. Earth Planet. Sci. Lett. 366, 6–16.
Nimmo, F., Agnor, C.B., 2006. Isotopic outcomes of N-body accretion simulations: Constraints on equilibration processes during large impacts from Hf/W observations. Earth Planet. Sci. Lett. 243, 26–43.
Nimmo, F., Kleine, T., 2007. How rapidly did Mars accrete? Uncertainties in the Hf–W timing of core formation. Icarus 191, 497–504.
Nimmo, F., O'Brien, D.P., Kleine, T., 2010. Tungsten isotopic evolution during late-stage accretion: Constraints on Earth–Moon equilibration. Earth Planet. Sci. Lett. 292, 363–370.
O'Brien, D.P., Morbidelli, A., Levison, H.F., 2006. Terrestrial planet formation with strong dynamical friction. Icarus 184, 39–58.
O'Neill, H.S.C., Palme, H., 2008. Collisional erosion and the non-chondritic composition of the terrestrial planets. R. Soc. Lond. Philos. Trans. Ser. A 366, 4205–4238.
Pahlevan, K., Stevenson, D.J., 2007. Equilibration in the aftermath of the lunar-forming giant impact. Earth Planet. Sci. Lett. 262, 438–449, 1012.5323.
Raymond, S.N., Quinn, T., Lunine, J.I., 2006. High-resolution simulations of the final assembly of Earth-like planets I. Terrestrial accretion and dynamics. Icarus 183, 265–282.
Rubie, D.C. et al., 2011. Heterogeneous accretion, composition and core–mantle differentiation of the Earth. Earth Planet. Sci. Lett. 301, 31–42.
Rubie, D.C., Melosh, H.J., Reid, J.E., Liebske, C., Righter, K., 2003. Mechanisms of metal-silicate equilibration in the terrestrial magma ocean. Earth Planet. Sci. Lett. 205, 239–255.
Rubie, D.C., Jacobson, S.A., Morbidelli, A., O'Brien, D.P., Young, E.D. Nimmo, F., Palme, H., Frost, D., 2014. Accretion and differentiation of the terrestrial planets with implications for the compositions of early-formed Solar System bodies and accretion of water. Icarus (submitted for publication).
Rudge, J.F., Kleine, T., Bourdon, B., 2010. Broad bounds on Earth's accretion and core formation constrained by geochemical models. Nature Geosci. 3, 439–443.
Russell, C.T. et al., 2012. Dawn at Vesta: Testing the protoplanetary paradigm. Science 336, 684–686.
Sarid, G., Stewart, S.T., Leinhardt, Z.M., 2014. Mercury, the impactor. Lunar Planet. Sci. Abstract #2723.
Sasaki, T., Abe, Y., 2007. Rayleigh–Taylor instability after giant impacts: Imperfect equilibration of the Hf–W system and its effect on the core formation age. Earth Planets Space 59, 1035–1045.
Schönbächler, M., Carlson, R.W., Horan, M.F., Mock, T.D., Hauri, E.H., 2010. Heterogeneous accretion and the moderately volatile element budget of Earth. Science 328, 884–887.
Siebert, J., Badro, J., Antonangeli, D., Ryerson, F.J., 2013. Terrestrial accretion under oxidizing conditions. Science 339, 1194–1197.
Stewart, S.T., Leinhardt, Z.M., 2012. Collisions between gravity-dominated bodies. II. The diversity of impact outcomes during the end stage of planet formation. Astrophys. J. 751, 32:1–32:17.
Walsh, K.J., Morbidelli, A., Raymond, S.N., O'Brien, D.P., Mandell, A.M., 2011. A low mass for Mars from Jupiter's early gas-driven migration. Nature 475, 206–209.
Wood, B.J., Walter, M.J., Wade, J., 2006. Accretion of the Earth and segregation of its core. Nature 441, 825–833.